

# Projected sea level rise, gyre circulation and water mass formation in the western North Pacific: CMIP5 inter-model analysis

Mio Terada<sup>1</sup> · Shoshiro Minobe<sup>1</sup>

Received: 28 November 2016 / Accepted: 6 September 2017 / Published online: 13 September 2017  
© Springer-Verlag GmbH Germany 2017

**Abstract** Future changes in the dynamic sea level (DSL), which is defined as sea-level deviation from the global mean sea level, is investigated over the North Pacific, by analyzing data from the Coupled Model Intercomparison Project Phase 5. The analysis provides more comprehensive descriptions of DSL responses to the global warming in this region than available from previous studies, by using surface and subsurface data until the year 2300 under middle and high greenhouse-gas emission scenarios. The DSL changes in the North Pacific are characterized by a DSL rise in the western North Pacific around the Kuroshio Extension (KE), as also reported by previous studies. Subsurface density analysis indicates that DSL rise around the KE is associated with decrease in density of subtropical mode water (STMW) and with northward KE migration, the former (latter) of which is relatively strong between 2000 and 2100 for both RCP4.5 and RCP8.5 (between 2100 and 2300 for RCP8.5). The STMW density decrease is related to large heat uptake to the south and southeast of Japan, while the northward KE migration is associated with the poleward shift of the wind stress field. These features are commonly found in multi-model ensemble means and the relations among representative quantities produced by different climate models.

**Keywords** Dynamic sea level · CMIP5 climate models · Western North Pacific · Kuroshio Extension · Subtropical mode water · Global warming

## 1 Introduction

Sea-level rise due to global warming is an important issue for human society (see, among others, Lowe and Gregory 2006; Nicholls et al. 2014; Timmermann et al. 2010; Willis and Church 2012). In the Fifth Assessment Report of the Intergovernmental Panel on Climate Change (IPCC-AR5), the future global mean sea-level rise in the 2081–2100 period, relative to the 1986–2005 period, is estimated as 0.47 m (0.32–0.63 m of 90% likely range) and 0.63 m (0.45–0.82 m of 90% likely range) for the middle and high greenhouse-gas emission scenarios in Representative Concentration Pathways (RCP) 4.5 and RCP8.5, respectively (Church et al. 2013). An updated assessment by Slangen et al. (2014) suggested higher values: 0.54 m for RCP4.5 and 0.71 m for RCP8.5. Because of continued ocean warming and further melting of the Greenland ice sheet, the global mean sea-level rise continues even when greenhouse-gas concentration is stabilized (Church et al. 2013).

Sea-level rise can be expressed as the sum of the global mean sea-level and a regional sea-level correction defined by the deviation of sea level in the region from the global mean. Regional sea-level change is characterized by the gravity adjustment of land-ice melt (Slangen et al. 2014), terrestrial water storage changes resulting from groundwater depletion (Wada et al. 2012), uplifting of the solid earth due to land-ice mass change (Mitrovica et al. 2011), long term glacial isostatic adjustment (Peltier 2004), non-uniform heat uptake by the ocean (e.g., Lowe and Gregory 2006; Suzuki and Ishii 2011b), and variation of ocean circulation (e.g., Gregory et al. 2001; Yin et al. 2010). Among these components, the last two involve complex dynamic and thermodynamic responses of the ocean to atmospheric forcing, and the difference in sea-level relative to the global mean attributable to these components is called the dynamic sea

✉ Mio Terada  
mio.terada@sci.hokudai.ac.jp

<sup>1</sup> Department of Natural History Sciences, Graduate School of Science, Hokkaido University, Science 8th bldg. 302, N10W8, Sapporo 060-0810, Japan

level (hereinafter, DSL) (e.g., Yin et al. 2010; Zhang et al. 2014). Better understanding of DSL for individual basins is needed for better understanding of sea-level rise issues. In this paper, we study future changes in DSL due to ocean properties (i.e., non-uniform heat uptake and variation of ocean circulation) for the North Pacific.

DSL change over the North Pacific due to global warming is characterized by relatively large sea-level rise in the western North Pacific to the east of Japan. This feature is commonly found in the multi-model ensemble (MME) mean of CMIP3 (Pardaens et al. 2010; Yin et al. 2010; Sueyoshi and Yasuda 2012; Zhang et al. 2014) as well as that of CMIP5 (Yin 2012; Church et al. 2013; Slangen et al. 2014). Since the location of the localized sea-level rise roughly corresponds to the Kuroshio and the Kuroshio Extension (KE), most previous studies have suggested that the rise is related to these currents (Yin et al. 2010; Sueyoshi and Yasuda 2012; Zhang et al. 2014; Liu et al. 2016). Analyzing multiple models of CMIP3, Sueyoshi and Yasuda (2012) reported that the meridional migration and strengthening of the KE each contribute to the regional sea-level change, but these two modes of the KE change occur differently in different models. The northward migration of the KE is associated with the northward shift of the latitude of zero Sverdrup stream function (SSF), which gives the boundary between the subtropical and subpolar gyres of wind-stress-forced circulations in linear models. This is consistent with another CMIP3 analysis by Zhang et al. (2014) and downscaling of three CMIP5 models by Liu et al. (2016). The poleward shift of the zero-SSF line is closely associated with the northward move of the Aleutian Low (Sueyoshi and Yasuda 2012), and is probably related to the northward expansion of the mean atmospheric circulation, including the Hadley cell (Miller et al. 2006; Rauthe et al. 2004; Collins et al. 2013).

In addition to wind forcings, anomalous heat flux to the ocean can be important in localized sea-level rise in the western North Pacific. Using a series of experiments with a climate model, Suzuki and Ishii (2011a) suggested that large heat uptake, via surface heat flux, in the subtropical mode water (STMW) lowers density of that water mass, resulting in a larger sea-level rise over it. This explanation is consistent with an earlier modeling experiment by Lowe and Gregory (2006). Furthermore, Suzuki and Ishii (2011b) reported that warming and freshening of STMW has played an important role in sea-level rise around the subtropical gyre in the North Pacific over the last three decades by using gridded temperature and salinity data from Ishii and Kimoto (2009).

Further studies are important to better understanding of future DSL changes over the North Pacific. The potential role of heat uptake of STMW has not been investigated in previous multi-model analyses. Moreover, few previous studies of DSL change over the North Pacific using

multi-model data of CMIP3 or CMIP5 have analyzed the differences among models. The study by Sueyoshi and Yasuda (2012) is a notable exception, but that analysis is limited to only the twenty-first century under the middle scenario of the IPCC Special Report on Emission Scenarios (SRES) A1B and does not consider subsurface density and velocity fields. Therefore, expanding analysis to multiple scenarios and to a longer time duration (up to the twenty-third century, for which some of CMIP models are available) and including subsurface density and velocity fields will clearly advance understanding of sea-level rise. Toward that end, the purpose of this study is to provide a more comprehensive description and an improved mechanism for assessment of future DSL changes over the North Pacific by analyzing model dependency using multiple climate models of CMIP5. In this study, we analyze both the middle scenario (RCP4.5) and the high scenario (RCP8.5) until the twenty-third century, using the outputs of more than 30 climate models for the twenty-first century. This is more than double the 15 models used by Sueyoshi and Yasuda (2012) the 11 models used by Zhang et al. (2014).

The rest of the paper is organized as follows. Section 2 describes the climate models and method used in this study. Section 3 examines DSL change and the associated change of density and velocity in the subsurface ocean. Section 4 analyzes how DSL changes are related to surface forcings. Section 5 presents a discussion and summary.

## 2 Data and methods

The outputs used in this study, which come from climate models participating in CMIP5 (Taylor et al. 2012), are obtained mainly through the Program for Climate Model Diagnosis and Intercomparison (<http://cmip-pcmdi.llnl.gov/cmip5/>). We used model outputs for the historical experiment up to December 2005 and those for the high- and medium-emissions scenarios of RCP8.5 and RCP4.5, respectively, for January 2006–December 2300. Outputs of RCP2.6 and RCP6.0 are not analyzed in this study because of the relatively smaller number of available models. Green-house gas concentration and thus radiative forcing stabilizes shortly after 2100 in RCP4.5 (Thomson et al. 2011), and in 2240 in RCP8.5 (Liddicoat et al. 2012). We used outputs of 34 (32) models for RCP8.5 (RCP4.5) until 2100 and of 6 models until 2300. Heat flux data (*hfds* from CMIP5) are available to the authors from the 23 (9) listed models for RCP8.5 (RCP4.5). We used only the first ensemble of each model so as to treat all models equally. All model outputs are interpolated to a common horizontal grid with  $1^\circ \times 1^\circ$  resolution for estimating the MME, and the three-dimensional temperature and salinity data are also interpolated to a common set of 28 vertical levels.

The DSL was defined as the sea level relative to the global mean sea level of CMIP5 models ( $z_{OS}$  from CMIP5). As mentioned above, DSL includes neither glacial isostatic adjustment nor gravitational adjustment of land-ice melt and change in land water storage. The inverted barometer effect is not considered because the DSL change related to atmospheric pressure change is much smaller than the steric and DSL change (Slangen et al. 2014).

To understand how sea-level changes are related to density changes at depth, the contribution of the steric component to DSL change is estimated. Sea level can be generally decomposed into steric and mass components

(Yin et al. 2010; Zhang et al. 2014; Liu et al. 2016). The sea-level differences due to the steric effect between two epochs ( $\Delta\eta$ ) is given by using the hydrostatic balance:

$$\Delta\eta = -\frac{1}{\rho_0} \int_{h_{REF}}^0 \Delta\rho dz, \tag{1}$$

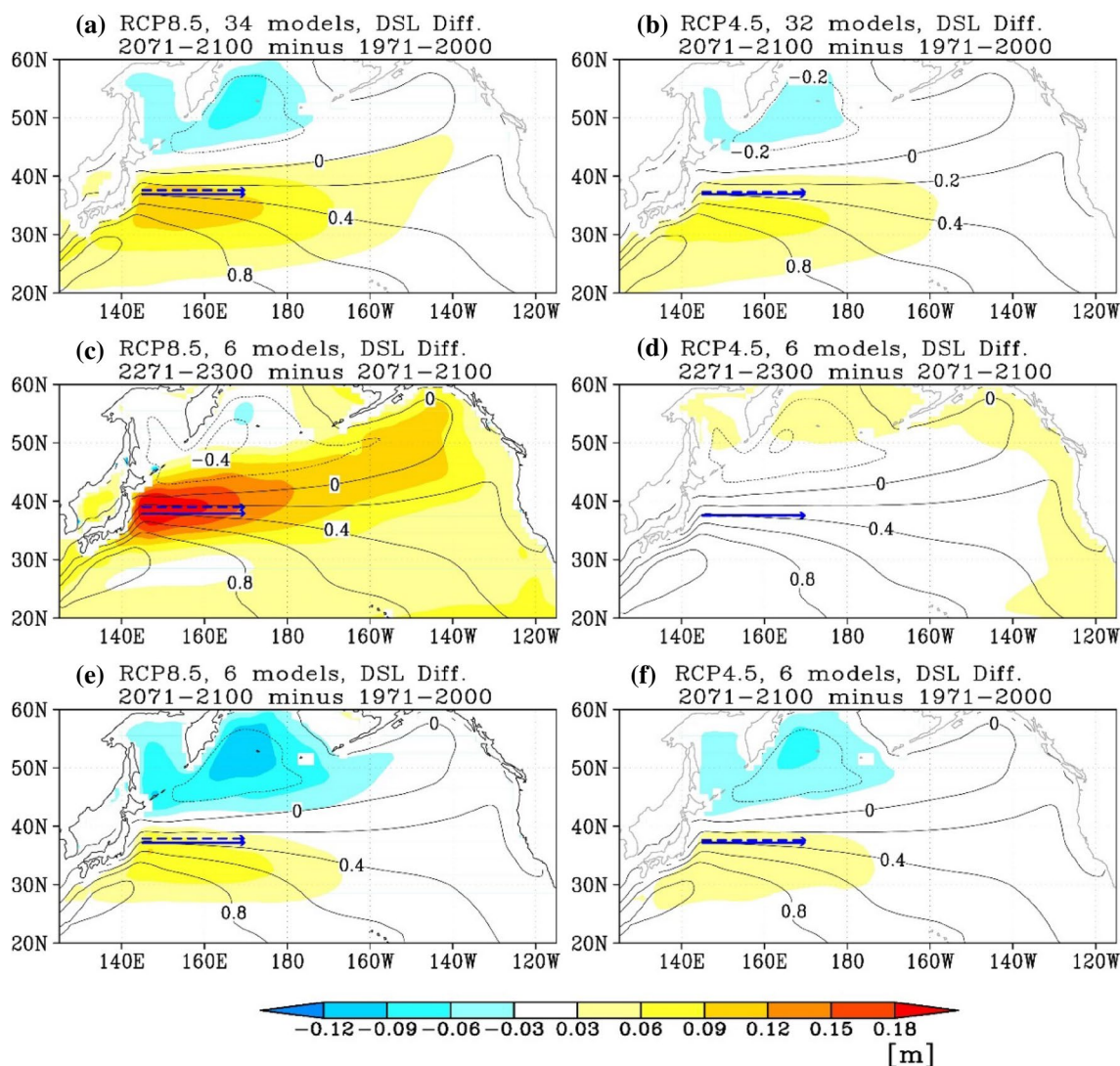


**Fig. 1** DSL differences (color) **a** between 1971 and 2000 and 2071–2100 periods for 34-model MME under RCP8.5, **b** between 1971 and 2000 and 2071–2100 periods for 32-model MME under RCP4.5, **c** between 2071 and 2100 and 2271–2300 periods for 6-model MME under RCP8.5, and **d** between 2071 and 2100 and 2271–2300 periods for 6-model MME under RCP4.5. Panel **e**, **f** is same as **a**, **b** but for 6-model MME. Contours indicate the mean DSL for the peri-

ods of **(a, b, d, f)** 1971–2000 and **(c, d)** 2071–2100. Solid (dashed) blue arrows indicate the KE axis latitude for the periods of **(a, b, e, f)** 1971–2000 (2071–2100) and **(c, d)** 2071–2100 (2271–2300). The KE axis latitude is estimated as the center of gravity of eastward geostrophic surface velocity, zonally averaged over 145°–170°E, 25°–50°N

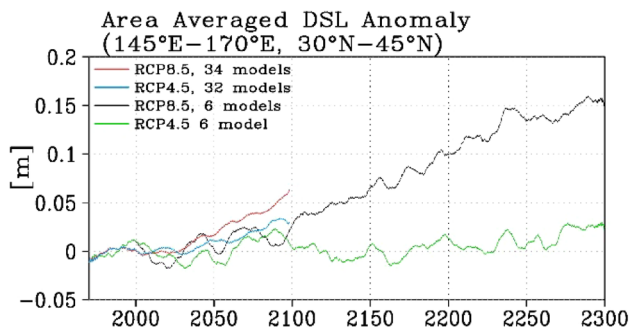


**Fig. 2** Time series of the area-averaged (145°–170°E, 30°–45°N) DSL anomaly from 1971 to 2000 mean smoothed by applying an 11-year running mean for 34-model MME under RCP8.5 (red), 32-model MME under RCP4.5 (blue), 6-model MME under RCP8.5 (black), and 6-model MME under RCP4.5 (green)

where  $\Delta\rho$  is the in-situ density difference,  $h_{REF}$  is the reference depth and  $\rho_0$  is the reference density. The reference depth is set to 2000 m, and the reference density is set to 1025 kg/m<sup>3</sup>. To understand the density changes corresponding to DSL, we introduce local density, which is defined by the density relative to the global mean density at each depth. This approach allows us to examine how DSL is related to the three-dimensional density structure at each depth in

more detail than allowed by the approach employed by Yin et al. (2010), who defined local steric sea-level rise after calculating steric sea-level by vertical integration of densities.

We also calculate the geostrophic velocities using in-situ densities, calculated from temperature and salinity, and sea surface heights on a 1° × 1° grid. Surface velocities are obtained from sea surface height with geostrophic balance assumption, and subsurface velocities are calculated by integrating the thermal wind equation from the surface to downward without an assumption of a level of no motion. It is noteworthy that publicly available CMIP5 data have velocity components only in the original coordinate system of the model, without information on the angles of coordinates relative to the meridian. This makes it difficult to obtain zonal and meridional components of velocities from CMIP5 outputs by coordinate rotation. Despite this, by using geostrophic velocities, we can assess changes in subsurface oceanic circulation.

### 3 DSL and density changes

The spatial structure of DSL changes differs before and after 2100. Until 2100, changes are characterized by a meridional dipole accompanying DSL rises (falls) in the subtropical

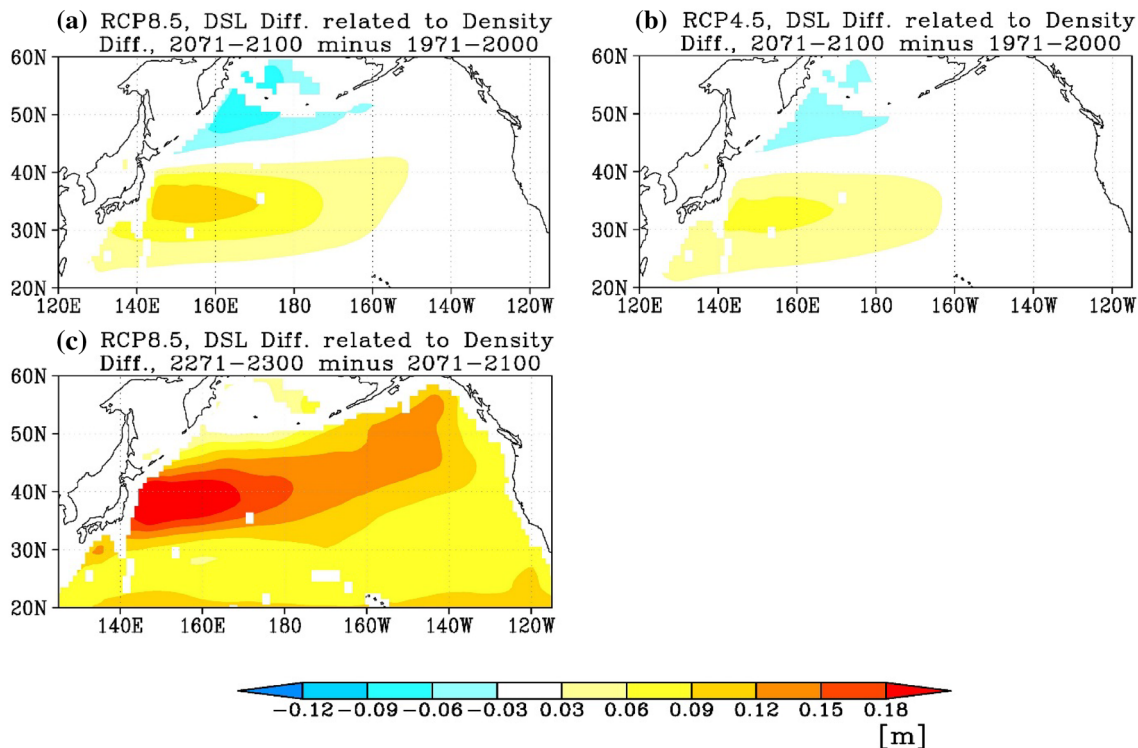


**Fig. 3** Same as Fig. 1 a–c, but for local steric sea-level differences



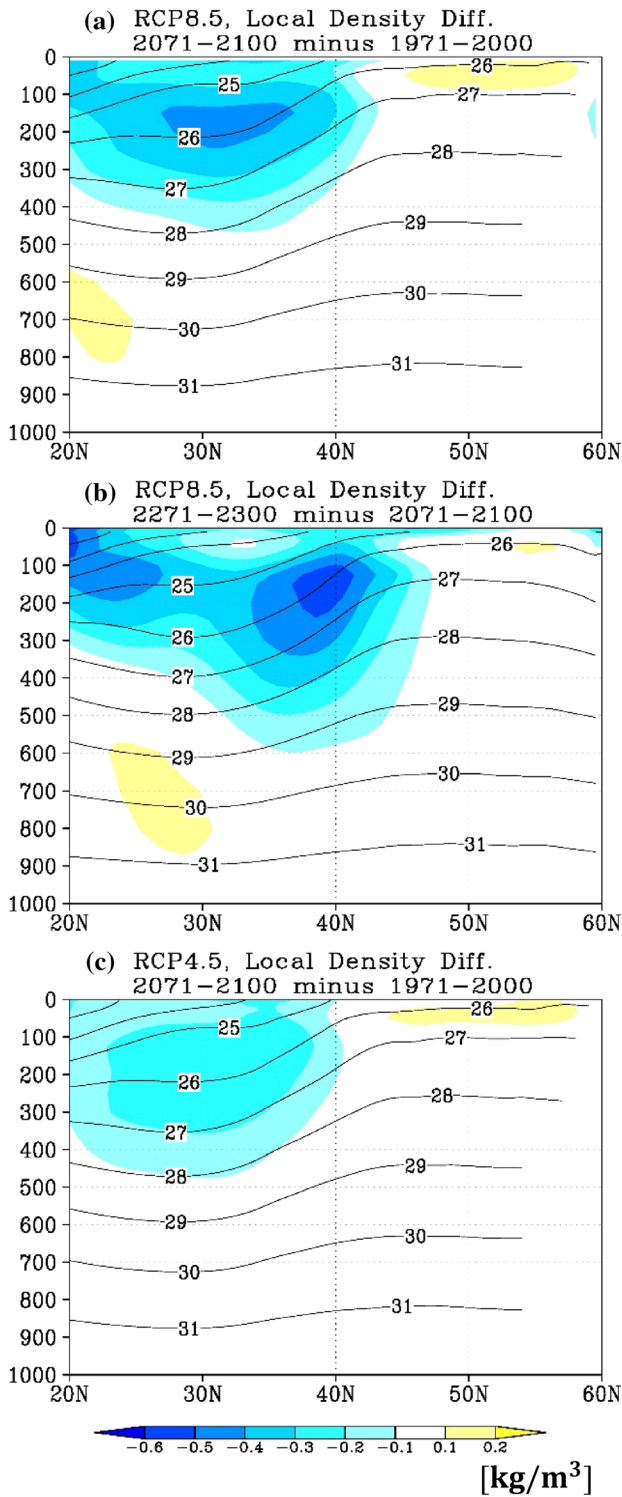


**Fig. 4** Zonally averaged ( $145^{\circ}$ – $170^{\circ}$ E) local density differences (color) **a** between 1971 and 2000 and 2071–2100 periods for 34-model MME under RCP8.5, **b** between 2071 and 2100 and 2271–2300 periods for 6-model MME under RCP8.5, and **c** between 1971 and 2000 and 2071–2100 periods for 32-model MME under RCP4.5. Local density is defined as the deviation from global mean density at each level (see text). Contours indicate the mean  $\sigma$  for the periods (**a**), **c**) 1971–2000 and **b**) 2071–2100

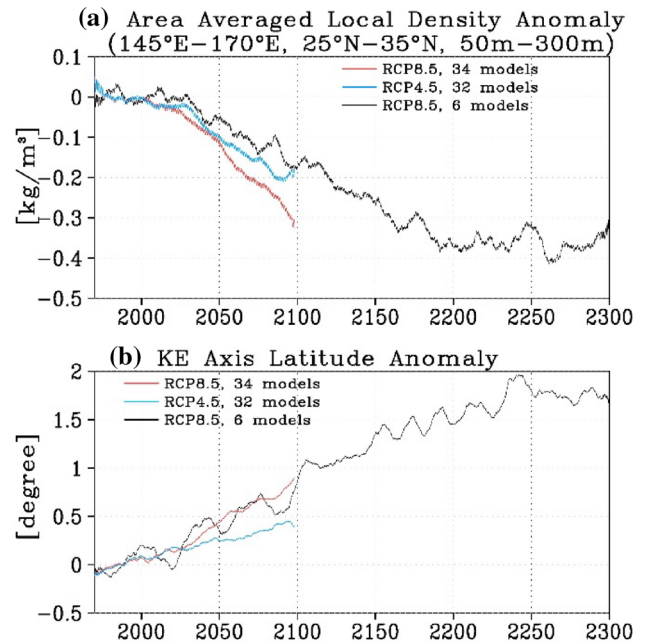


**Fig. 5** Time series of **a**) local density anomaly averaged in the STMW region ( $145^{\circ}$ – $170^{\circ}$ E,  $25^{\circ}$ N– $35^{\circ}$ N, and depth 50–300 m) and **b**) the KE-axis latitude anomaly smoothed by applying an 11-year running mean for 34-model MME under RCP8.5 (red), 32-model MME under RCP4.5 (blue), and 6-model MME under RCP8.5 (black)

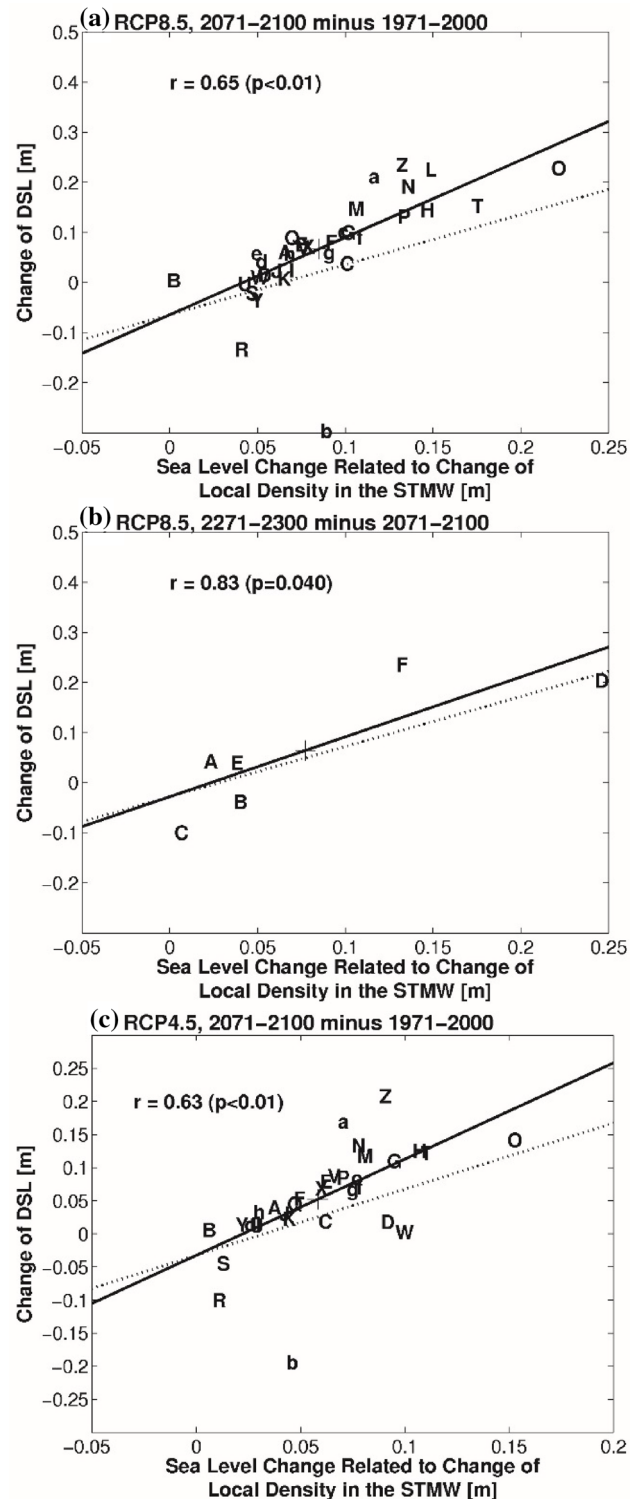
(subpolar) gyre in the western North Pacific for both the RCP4.5 and RCP8.5 scenarios (Fig. 1a, b). This is consistent with previous studies using CMIP5 models (Yin 2012; Church et al. 2013; Slangen et al. 2014) and CMIP3 models (e.g., Sueyoshi and Yasuda 2012; Zhang et al. 2014). These patterns are somewhat (completely) different from the DSL change pattern for RCP8.5 (RCP4.5) from 2100 to 2300. For RCP8.5, the strong DSL rise to the east of Japan between 2100 and 2300 is shifted northward from that between 2000 and 2100, exhibiting a monopole pattern over the basin (Fig. 1c). The maximal DSL rise between the twentieth and twenty-first centuries is 11 cm, occurring near the KE east of Japan, and is 23 cm between the twenty first and twenty third centuries for RCP8.5. In contrast, DSL changes after 2100 for RCP4.5 are very weak around the KE, and slightly positive in the eastern and northern North Pacific (Fig. 1d). The changed structure before and after 2100 is not due to different ensemble sizes (30+ vs 6): the pattern of DSL changes before 2100 identified from the MME of six models that are available through the twenty third century is essentially the same as found with a larger number of models used to produce Fig. 1a, b (Fig. 1e, f).

Time series of area-averaged DSL anomaly from the 1971–2000 mean around the KE over  $30^{\circ}$ – $45^{\circ}$ N and  $145^{\circ}$ – $170^{\circ}$ E are generally consistent with the temporal evolution of radiative forcing in each scenario. The time series from RCP8.5 exhibits faster and longer lasting increases

**Fig. 6** Scatter diagram of epoch differences in DSL due to local density averaged in the STMW region (145°–170°E, 25°–35°N, and depth 50–300 m) and DSL over the same domain among climate models. The epochs and scenarios are **a** 1971–2000 and 2071–2100 periods under RCP8.5, **b** 2071–2100 and 2271–2300 periods under RCP8.5, and **c** 1971–2000 and 2071–2100 periods under RCP4.5. The plus symbol (+) and alphabetical letters denote the MME and the models (Table 1), respectively. Correlation coefficients and  $p$  values are shown in the panels. Solid lines indicate regression lines, while dotted lines denote the lines of slope 1

than seen from RCP4.5 (Fig. 2). The DSL anomaly is rather stable during the end of the twentieth century and the early twenty-first century, and then starts increasing before 2050 for both scenarios. These results for 30+ models are statistically robust, because the 5–95% likely range of 30-year mean MME DSL for each periods are smaller than  $\pm 10\%$  of its value. The area-averaged DSL anomaly appears to continuously increase until around the end of the twenty-first century for RCP4.5 and until the end of the twenty-third century for RCP8.5, but internal variability from individual model is remained in 6-model MMEs because of the small ensemble size. Since DSL change in RCP4.5 is weak after 2100, we analyze RCP4.5 only before 2100.

The DSL changes shown in Fig. 1 are quite well explained by the steric component (Fig. 3). Thus, the DSL change over the North Pacific is dominated by the steric sea-level change. This is consistent with the findings of Yin et al. (2010), who showed that the steric component is dominant in the open ocean. To better understand how three-dimensional density changes are related to DSL changes, we examine local density, which is defined as the density relative to the global mean density at each depth, as mentioned in Sect. 2 (Fig. 4). We focus our attention to DSL changes east of Japan, where large DSL changes are found until 2100 under both scenarios and until 2300 in the RCP8.5 scenario, as shown in Fig. 1. Until 2100, the local density decrease is centered around 30°N between depths of 100 and 300 m (Fig. 4a, c). In this region, the climatological vertical density gradient is weak, as shown by the wider distance between the  $\sigma$  (1000 kg/m<sup>3</sup> is subtracted from in-situ density) contours of 25 and 27 kg/m<sup>3</sup> for the end of the twentieth century, indicating the presence of STMW. This means that the decreases in local density occur in the STMW, locating over the southern flank of KE and further south. In contrast, after 2100, the local density decrease has its maximum around 39°N, corresponding to the KE axis rather in the STMW region (Fig. 4b). The large negative change in local density near the KE axis suggests its northward migration. Although the density decreases in the region of STMW and near the KE axis occur in both the twenty-first and twenty-second to twenty-third centuries, the density decreases more strongly in the region of STMW than around the KE axis until 2100 under both RCP4.5 and RCP8.5. Furthermore, the density decreases more strongly



around the KE axis than in the STMW region after 2100 under RCP8.5. The density decrease in the STMW is accompanied by a temperature increase (not shown), which suggests that heat uptake associated with the STMW plays an important role in DSL change, as suggested by Suzuki and Ishii (2011b). It is interesting to note that Sugimoto et al.

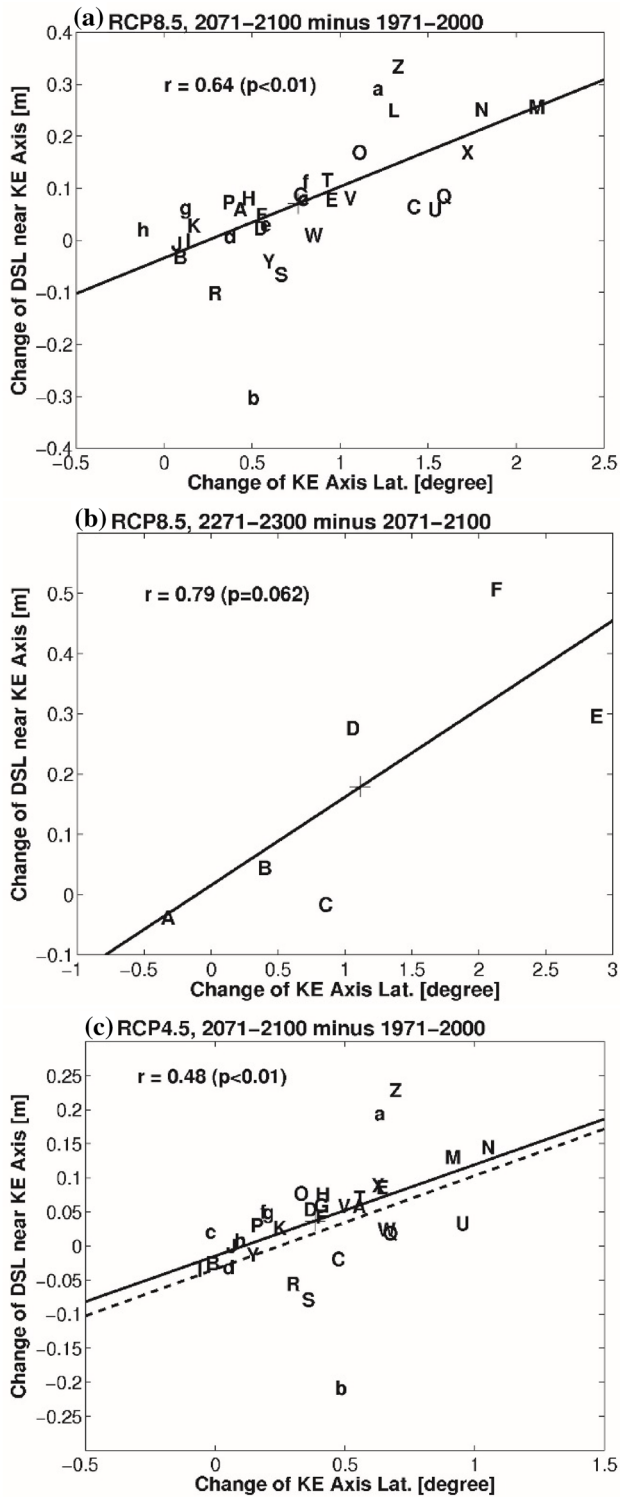


**Fig. 7** As in Fig. 6, but for epoch differences of KE axis latitude and DSL around the KE axis (145°–170°E, 35°–40°N) among climate models. The dashed line in **c** is the regression line from **a**

(2017) very recently reported that an enhanced warming of the STMW under the global warming may have already occurred over the past six decades.

The MME time series of volume-averaged local density anomaly for the STMW and for the KE axis latitude anomaly exhibit negative and positive trends, respectively (Fig. 5). The KE axis latitude is estimated as the center of gravity of eastward geostrophic surface velocity, zonally averaged over 145°–170°E, 25°–50°N with westward velocities being ignored. Before the 2000s, the time series of STMW density anomaly is roughly stable, but the KE axis latitude appears to start migrating northward before 2000.

Next, we investigate whether these relations we found in MME are common for all models, and if so, we determine how strongly each variables can explain the DSL differences among models. Figure 6 shows the relation between DSL changes resulting from changes in STMW density and the DSL changes generally in the region of STMW. The regression slopes are close to unity (1.54 and 1.45 for RCP8.5 and RCP4.5, respectively for 30+ models), and the correlations are strong ( $r = 0.63$ – $0.83$ ), indicating that the local decrease of density in the STMW well explains the DSL rise there for both periods and scenarios. Figure 7 shows changes of the KE axis latitude plotted against DSL differences averaged over 145°–170°E, 35°–40°N which contains the KE axis latitudes during the analysis period. The DSL differences are significantly correlated with the northward migration of the KE latitude. The relationship becomes stronger as the greenhouse-gas emissions accumulate (and thus radiative forcing increases) across different scenarios and periods. This is a new finding obtained by the analysis of multiple scenarios until 2300.

The association between DSL changes and velocity changes at depth is a topic of interest for this study. Figure 8 shows that the eastward flow increase (decrease) in the northern (southern) side of the KE, independently of scenario and period, is consistent with the northward KE migration. Another interesting feature is that the velocity changes contains signature of shallowing, which is more clearly seen in the vertical profile of the horizontally averaged zonal geostrophic velocity (Fig. 9a). This is associated with velocity weakening in deeper levels, probably because of enhanced upper ocean stratification due to surface warming and freshening (Fig. 9b).

#### 4 Atmospheric forcing

In this section, we analyze heat flux and wind stress to show how external forcings of the ocean cause changes in DSL. We focus particular attention on how these forcings influence density reduction of the STMW and northward migration of the KE, which were documented in the previous section.

**Table 1** CMIP5 models used in this study. HF indicates that downward net heat flux data (*hfds* in CMIP5) were available to the authors

	Model	Country	2100 RCP8.5 (34 models)	2100 RCP4.5 (32 models)	2300 RCP8.5 (6 models)	2300 RCP4.5 (6 models)
A	BCC-CSM1-1	China	✓ (HF)	✓	✓ (HF)	✓
B	CNRM-CM5	France	✓ (HF)	✓	✓ (HF)	✓
C	GISS-E2-R	USA	✓ (HF)	✓	✓ (HF)	✓
D	HadGEM2-ES	UK	✓	✓	✓	✓
E	IPSL-CM5A-LR	France	✓	✓	✓	✓
F	MPI-ESM-LR	Germany	✓ (HF)	✓ (HF)	✓ (HF)	✓ (HF)
G	ACCESS1-0	Australia	✓ (HF)	✓		
H	ACCESS1-3	Australia	✓ (HF)	✓		
I	BCC-CSM1-1-M	China	✓ (HF)	✓ (HF)		
J	CCSM4	USA	✓	✓		
K	CESM1-BGC	USA	✓	✓		
L	CESM1-WACCM	USA	✓	✓		
M	CMCC-CESM	Italy	✓ (HF)			
N	CMCC-CM	Italy	✓ (HF)	✓ (HF)		
O	CMCC-CMS	Italy	✓ (HF)	✓ (HF)		
P	CSIRO-Mk3-6-0	Australia	✓ (HF)	✓		
Q	CanESM2	Canada	✓	✓		
R	FGOALS-g2	China	✓ (HF)	✓ (HF)		
S	FGOALS-s2	China	✓ (HF)	✓		
T	FIO-ESM	China	✓ (HF)	✓		
U	GFDL-CM3	USA	✓	✓		
V	GFDL-ESM2G	USA	✓ (HF)	✓		
W	GFDL-ESM2M	USA	✓	✓		
X	HadGEM2-CC	UK	✓	✓		
Y	IPSL-CM5A-MR	France	✓	✓		
Z	IPSL-CM5B-LR	France	✓	✓		
a	MIROC-ESM	Japan	✓ (HF)	✓ (HF)		
b	MIROC-ESM-CHEM	Japan	✓ (HF)	✓ (HF)		
c	MIROC5	Japan	✓ (HF)	✓		
d	MPI-ESM-MR	Germany	✓ (HF)	✓ (HF)		
e	MRI-CGCM3	Japan	✓ (HF)	✓ (HF)		
f	MRI-ESM1	Japan	✓ (HF)			
g	NorESM1-M	Norway	✓ (HF)	✓		
h	NorESM1-ME	Norway	✓ (HF)	✓		

First, we examine the downward net heat flux (positive when ocean gains heat), which may be related to density change of the STMW (Suzuki and Ishii 2011a; Luo et al. 2009). We first calculate the heat flux anomaly in each year by subtracting its mean value of last 30 years in twentieth century, and then integrate it from 1971 to 2100 (Fig. 10a, b). The integrated downward heat flux anomaly is large in high latitudes (north of 50°N) and to the south and southeast of Japan. The former causes a large temperature increase in higher latitudes, but this heat uptake contributes less to local density, and thus to DSL, than in lower latitudes because

of the nonlinearity of the density equation for sea water. The mid-latitude positive integrated heat flux anomalies are located to the south of the climatological mean negative maximum (i.e., the location of maximum heat loss from the ocean over KE), and negative anomalies occur to the north of the climatological mean negative maximum. This spatial pattern represents northward migration of the heat flux field. It implies a link between the heat flux anomaly and northward migration of the KE. Area-averaged downward net heat flux continually increases south and southeast of Japan until



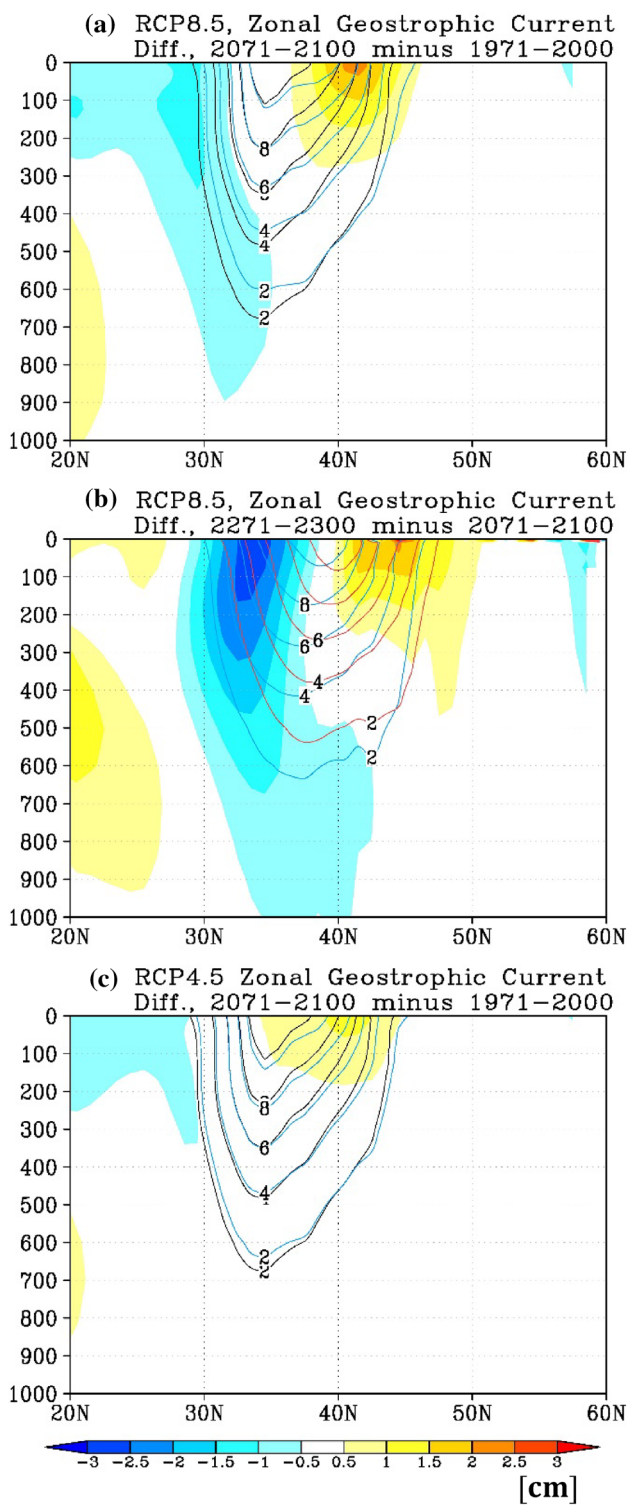


**Fig. 8** Eastward geostrophic current-speed differences, calculated using the zonally averaged (145°–170°E) in-situ density and sea level (color) **a** between 1971 and 2000 and 2071–2100 periods for 34-model MME under RCP8.5, **b** between 2071 and 2100 and 2271–2300 periods for 6-model MME under RCP8.5, and **c** between 1971 and 2000 and 2071–2100 periods for 34-model MME under RCP4.5. Black, blue, and red contours indicate the mean zonal geostrophic current speed for the periods 1971–2000, 2071–2100, and 2271–2300, respectively

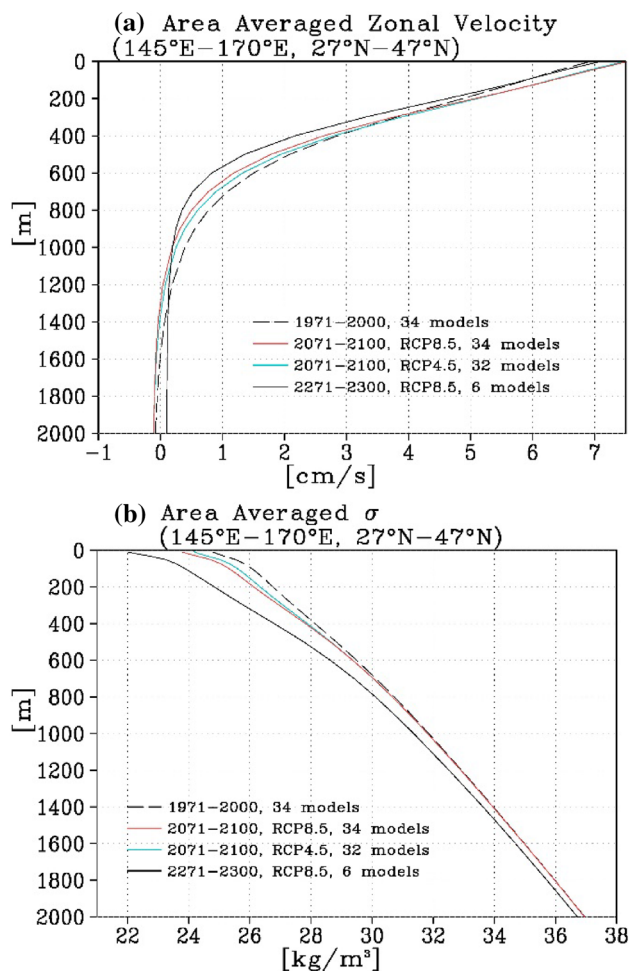


**Fig. 9** Vertical profiles of **a** zonal velocity and **b**  $\sigma$  averaged in 145°–170°E, 27°N–47°N for (black dashed curve) 1971–2000 period in the historical experiment, (red curve) 2071–2100 period under RCP8.5, (blue curve) 2071–2100 period under RCP4.5, and (black solid curve) 2272–2300 period under RCP8.5

the middle of the twenty-third (twenty-first) century for the RCP8.5 (RCP4.5) scenario (Fig. 10c).

The relation between changes in downward net heat flux and local density of the STMW is confirmed by analysis of differences among models (Fig. 11). Here, we limit our analysis of epochal differences, considering only between the ends of the twentieth and twenty-first centuries because we have only four models for which heat flux data are available until 2300, and this is too few for analysis of the relationship among models. Local density change in the STMW is negatively correlated with integrated downward heat flux anomalies south of Japan. Further investigation revealed that reduced atmospheric cooling in winter contributes more to STMW density decrease than increased atmospheric heating in summer (not shown). This means that anomalous ocean heat uptake in winter results in lighter water mass in the

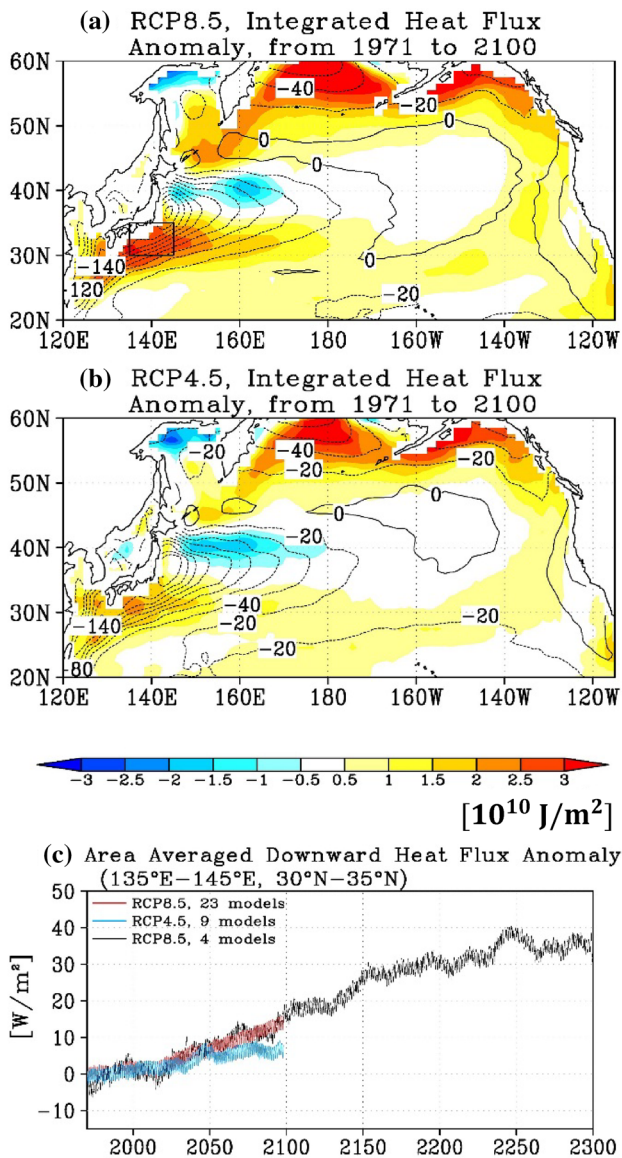


**Fig. 10** Time-integrated downward net heat flux anomaly (color) for **a** 23-model MME under RCP8.5 and **b** 9-model MME under RCP4.5. Panel **c** shows the time series of area-averaged downward net heat flux (130°–160°E, 25°–35°N) anomaly from 1971 to 2000 mean smoothed by applying an 11-year running mean for the following: (red) 23-model MME under RCP8.5, (blue) 9-model MME under RCP4.5, and (black) 4-model MME under RCP8.5. Contours in panels **a**, **b** indicate the mean downward net heat flux for the period 1971–2000. The domain for area averaging is marked by the box in **a**

STMW. As shown in the previous section, the lower density of this water mass is important in producing the maximal sea-level rise to the east of Japan.

The aforementioned possible link between the time-integrated downward heat flux anomaly to the south of Japan and northward KE migration is examined with various climate models (Fig. 12). The changes in downward net heat

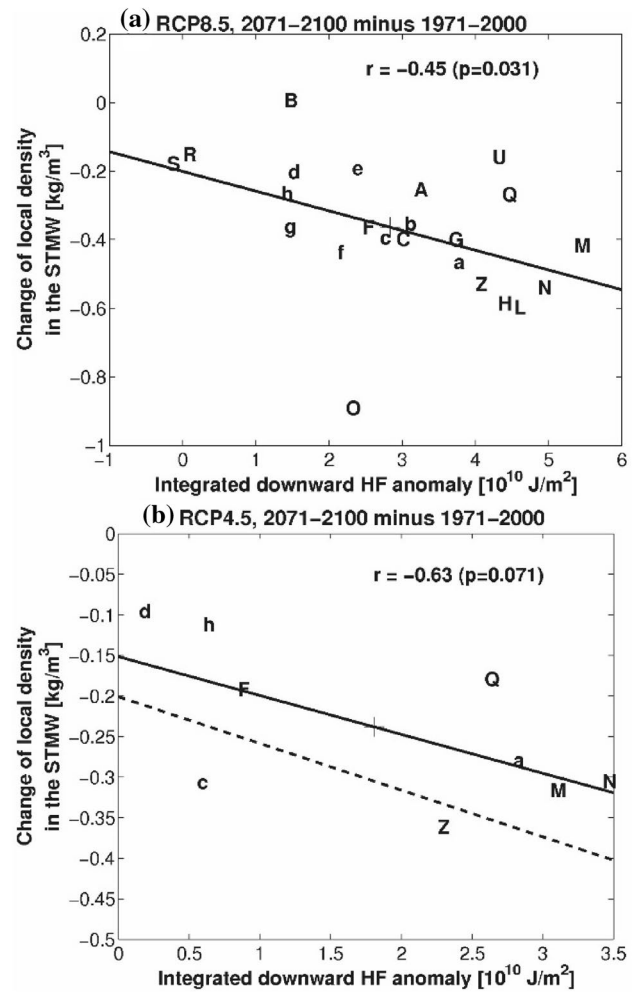


**Fig. 11** Scatter diagram of epoch differences of the local density averaged in the STMW region (145°–170°E, 25°–35°N, and depth 50–300 m) and integrated downward net heat flux averaged south of the KE (130°–160°E, 25°–35°N) among climate models between 1971 and 2000 and 2071–2100 periods. The scenarios are **a** RCP8.5 and **c** RCP4.5. The plus symbols (+) and alphabetical letters denote MME and the models (Table 1), respectively. Correlation coefficients and *p* values are shown. Solid lines indicate the regression line from the data points. The dashed line in **b** is the regression line from **a**

flux are strongly related to meridional migration of the KE axis latitude, with a correlation coefficient of 0.84 (0.95) for RCP8.5 (RCP4.5). This indicates that the northward KE migration is closely related to the anomalous heat flux south of Japan. Since downward heat flux takes its minimum along the KE axis (see contours of Fig. 10a, b), downward net heat flux will be increased (reduced) in the south (north) of its axis when it moves northward. Therefore, KE migration, integrated heat flux anomalies, and density changes of STMW are related. A possible causality is that the KE northward migration accounts for producing lighter water for the STMW through the anomalous ocean heat uptake south

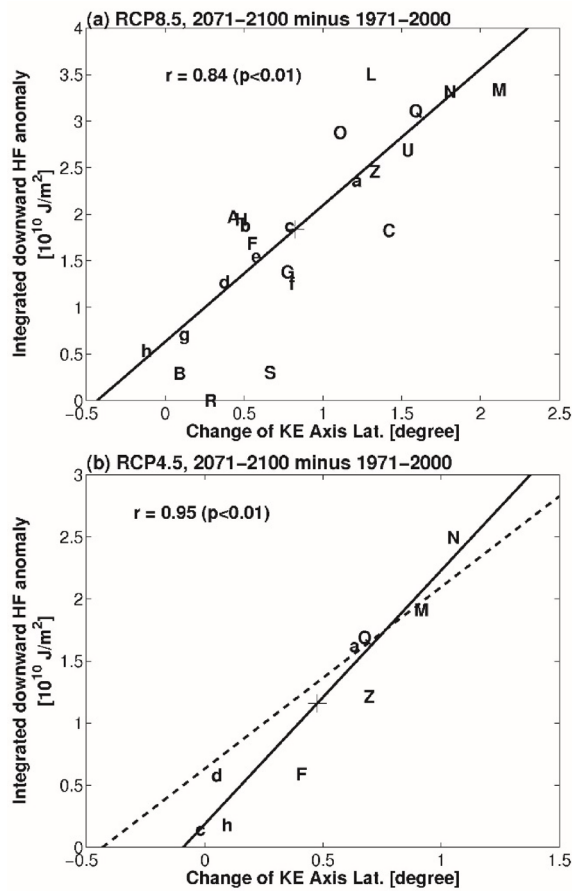


**Fig. 12** As in Fig. 11, but for epoch differences of the KE-axis latitude and integrated downward net heat flux averaged south of the KE (135°–145°E, 30°–35°N) among climate models. The dashed line in **b** is the regression line from **a**

of the KE axis until 2100. This chain of causality, however, is not dominant factor for STMW density change, because the correlation between the STMW density change and integrated heat flux anomaly is moderate ( $r = -0.45$  in Fig. 11a) and because the density decrease of STMW rather than the northward KE migration plays a more important role in DSL changes in the twenty-first century as mentioned above.

The meridional migration of the KE can be caused by variations of wind distribution because the KE participates in wind-driven circulation over the North Pacific. Figure 13a, b show the differences in zonal wind stress between the 1971–2000 and 2071–2100 periods under RCP8.5 and RCP4.5, respectively. Zonal wind stress is enhanced (weakened) to the north (south) of the climatological maximum zonal wind, centered around 40°N across the North Pacific, with stronger magnitudes for RCP8.5 than for RCP4.5. This spatial pattern indicates northward migration of the zonal wind stress field, consistent with previous studies (Sueyoshi and Yasuda 2012; Zhang et al. 2014). The wind stress curl field also exhibits northward migration of time-mean

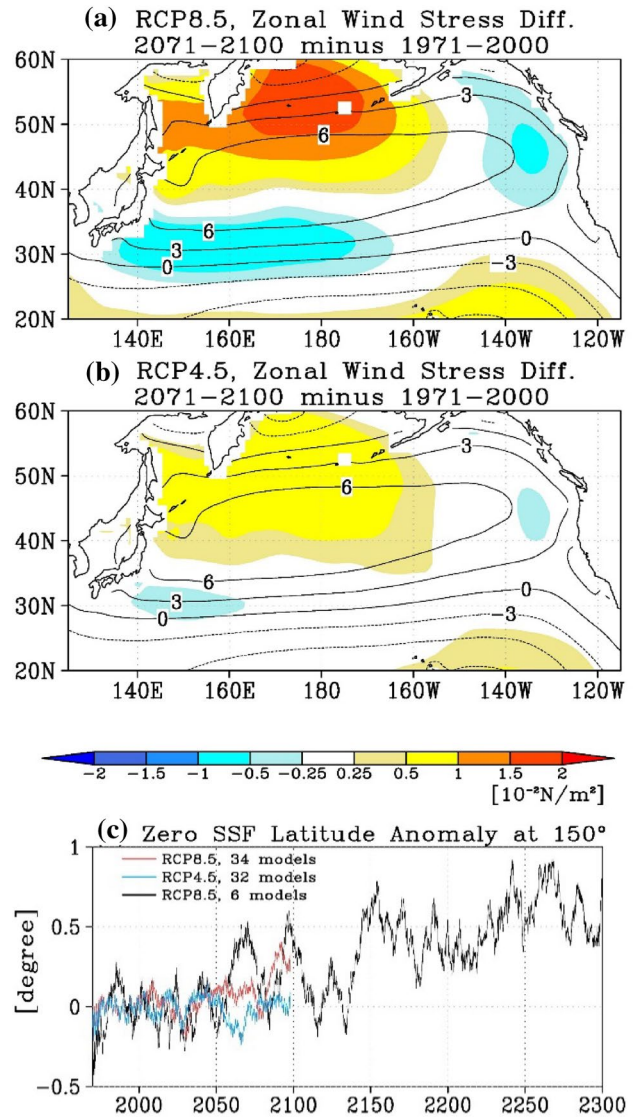


**Fig. 13** Zonal wind stress differences between 1971 and 2000 and 2071–2100 periods (color) **a** for 34-model MME under RCP8.5 and **b** for 32-model MME under RCP4.5. Contours indicate the mean zonal wind stress for the period 1971–2000. **c** Anomaly time series of the latitude of zero SSF at 150°E relative to 1971–2000 mean smoothed by applying an 11-year running mean for the following: (red) 34-model MME under RCP8.5, (blue) 32-model MME under RCP4.5, and (black) 6-model MME under RCP8.5. The SSF is calculated by zonally integrating wind stress curl westward from the eastern boundary (i.e., Sverdrup Balance)

pattern, and its change is characterized by an anticyclonic anomalies extending eastward from the east coast of Japan (not shown). The latitude of zonally averaged zonal wind stress maximum moves 1 (0.4) degrees to the north by 2100 in RCP8.5 (RCP4.5). Anomaly time series of the latitude of zero Sverdrup stream function (SSF) at 150° E over the North Pacific (150°E–160°W) exhibit northward movement until roughly the middle of the twenty-first (twenty-third



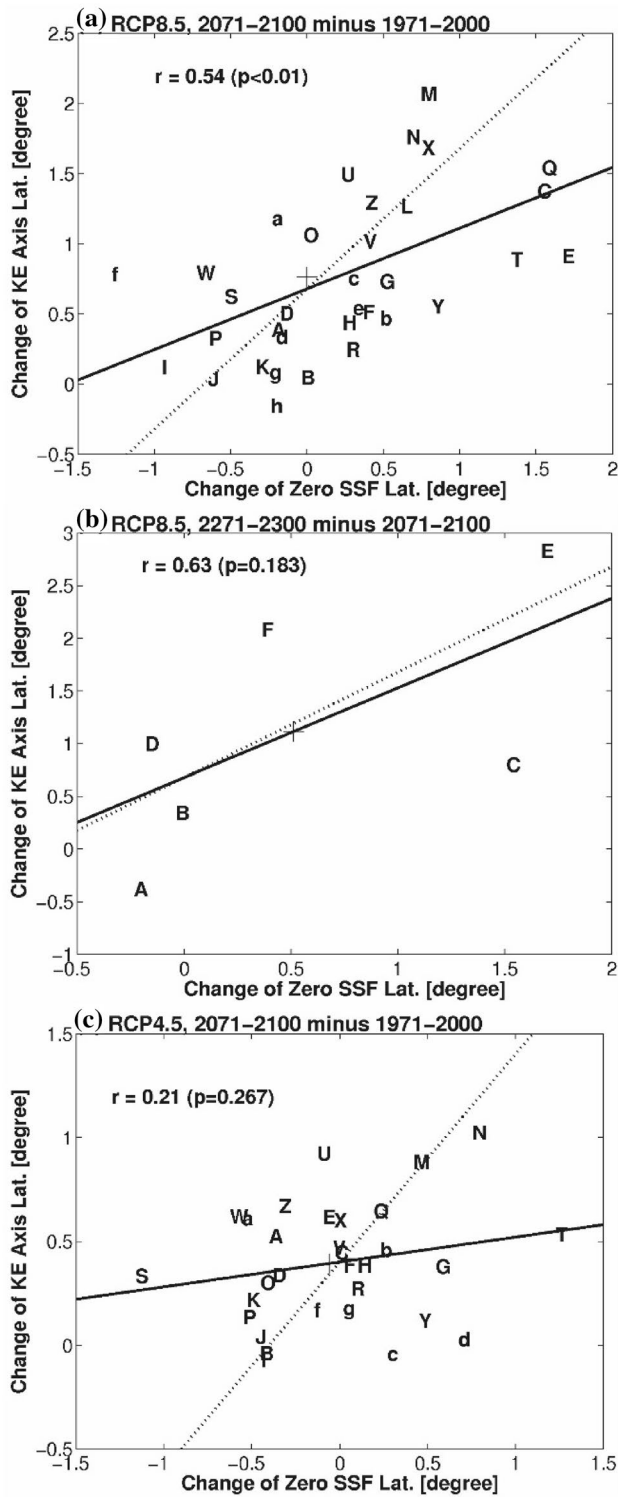


**Fig. 14** As in Fig. 6, but for epoch differences of the KE-axis latitude and the latitude of zero SSF at 150°E among climate models. Dotted lines indicate slope 1

century for RCP4.5 (RCP8.5) (Fig. 13c), though internal variability in each model is not averaged out especially in 6-model MME.

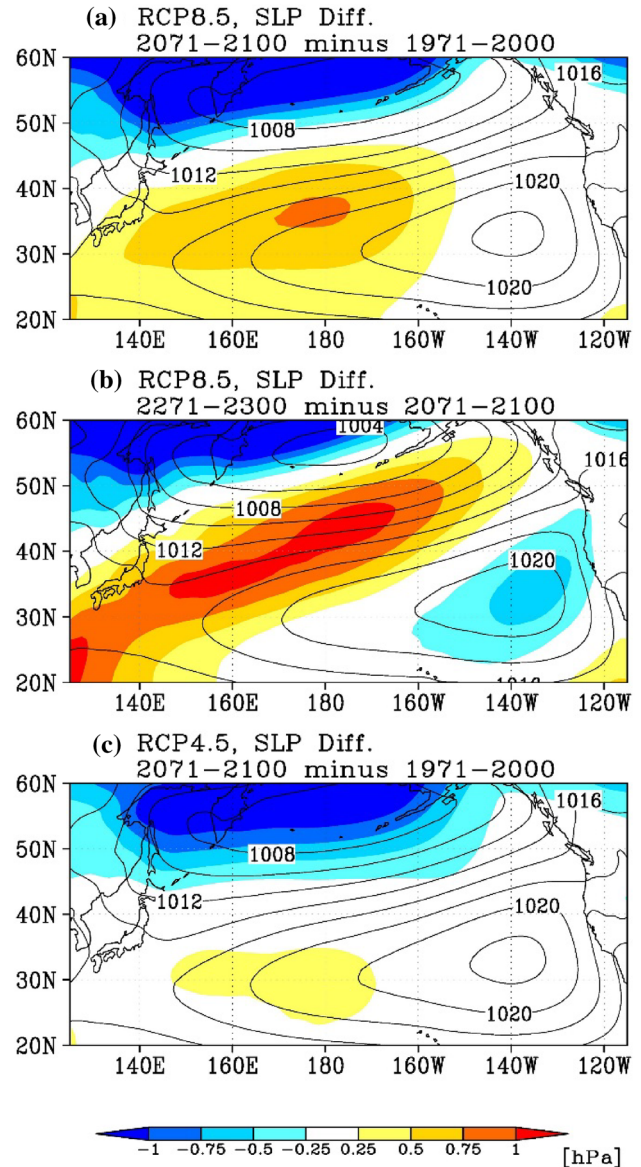


**Fig. 15** Epoch differences of SLP (color) **a** between 1971 and 2000 and 2071–2100 periods for 34-model MME under RCP8.5, **b** between 2071 and 2100 and 2271–2300 periods for 6-model MME under RCP8.5, and **c** between 1971 and 2000 and 2071–2100 periods for 32-model MME under RCP4.5. Contours indicate the mean SLP for the periods **a**, **c** 1971–2000 and **b** 2071–2100

Northward migration of the KE is significantly correlated (at the 5% significance) with that of the latitude of zero SSF under RCP8.5 ( $r = 0.54, p < 0.01$ ), but the correlation under RCP4.5 is not significant ( $r = 0.21, p = 0.27$ ) (Fig. 14). This means that although the MME indicates that both the KE axis and zero SSF latitude move northward, different KE migrations among models are not well explained by the shift in zero SSF latitude under RCP4.5. The stronger relationship in RCP8.5 relative to RCP4.5 suggests that the uncertainty



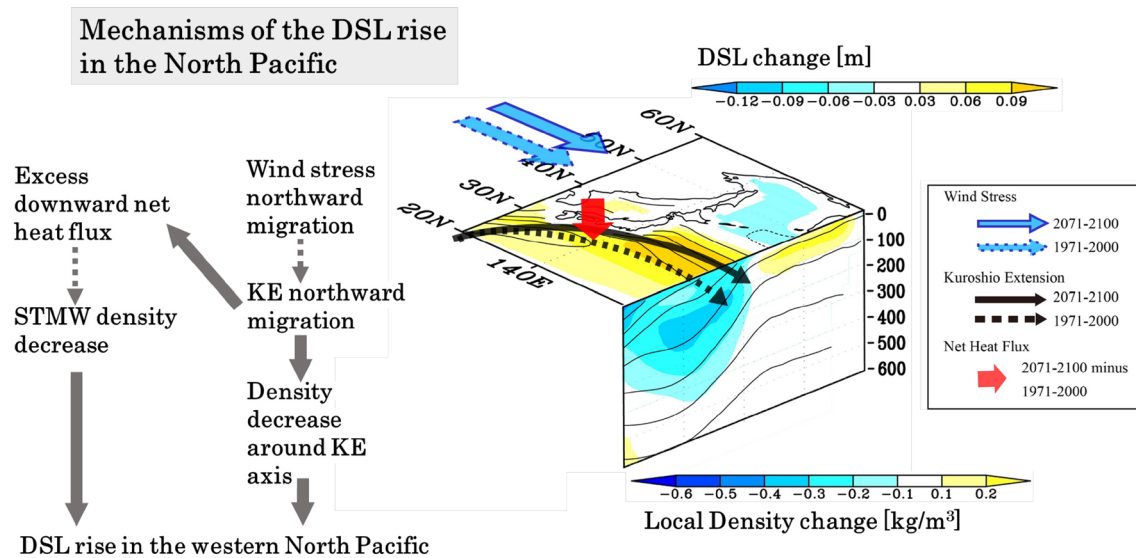


**Fig. 16** Schematic diagram illustrating the mechanism of DSL rise in the western North Pacific. DSL rises around the KE is associated with the density decrease of the STMW and northward KE migration. The STMW density decrease is caused by anomalous downward net heat flux to the south and southeast of Japan, while the northward KE migration is due to the poleward shift of the wind stress field. The

excess heat flux is also strongly related to the northward migration of the KE. The solid arrows indicate the inter-model relationships that are significant at 5% significance level for both the RCP4.5 and 8.5, while dashed arrows indicate the relationships that are significant only for RCP8.5 but not for RCP4.5

in RCP4.5 may arise from internal variability of the ocean, though further studies are necessary to clarify this. It is interesting to note that the regression slopes are all shallower than unity, meaning that the northward migration of the KE is smaller than migration of the zero SSF latitude in many models. This migration discrepancy may be due to a strong non-linearity of the KE, although its specific contribution is uncertain.

The northward migration of the SSF field and hence that of the zonal wind stress is likely influenced by the change of large-scale atmospheric circulation. Figure 15 shows the MME changes of sea-level pressure (SLP) over the North Pacific. Between the ends of the twentieth and twenty-first centuries, SLP changes are characterized by decreases in the Bering Sea and increases in the central and western North Pacific between 30°N and 40°N (Fig. 15a, c). This pattern of change in SLP indicates overall deepening and northward shifting of the Aleutian Low, consistent with previous studies (e.g., Sueyoshi and Yasuda 2012; Oshima et al. 2012; Collins et al. 2013; Gan et al. 2017). These changes to the Aleutian Low continue after 2100 and are accompanied by weakening of the subtropical high (Fig. 15b). The spatial patterns of changes in SLP are associated with positive trends of the annular modes as well as with poleward expansion of the Hadley circulation (Miller et al. 2006; Rauthe et al. 2004; Collins et al. 2013). These two phenomena may result from global warming (Cheon et al. 2012; Frierson

et al. 2007; Hu et al. 2013; Johanson and Fu 2009; Lu et al. 2007; Previdi and Liepert 2007).

### 5 Discussion and summary

We investigated change in DSL over the North Pacific until 2300 under middle and high greenhouse-gas emission scenarios (RCP4.5 and RCP8.5, respectively) by analyzing MME along with differences among models, including subsurface density and velocity fields, using output from CMIP5 models. This is the first study of subsurface density and velocity fields for the future DSL change in the western North Pacific. Hence, our analysis has provided more comprehensive understanding of future DSL changes.

The DSL changes in the North Pacific are characterized by DSL rise in the western North Pacific around the KE (Fig. 1), as reported in previous studies (Yin et al. 2010; Yin 2012; Sueyoshi and Yasuda 2012; Zhang et al. 2014; Church et al. 2013; Slangen et al. 2014). Around the KE, DSL continues to rise roughly through the twenty-first century under RCP4.5 and until the end of the twenty-third century under RCP8.5, indicating that DSL will continue to change for decades after stabilization of radiative forcing (Fig. 2). The localized DSL change around the KE is related to a density decrease of the STMW and to northward migration of the KE (Fig. 3). Both of them induce DSL rise in the

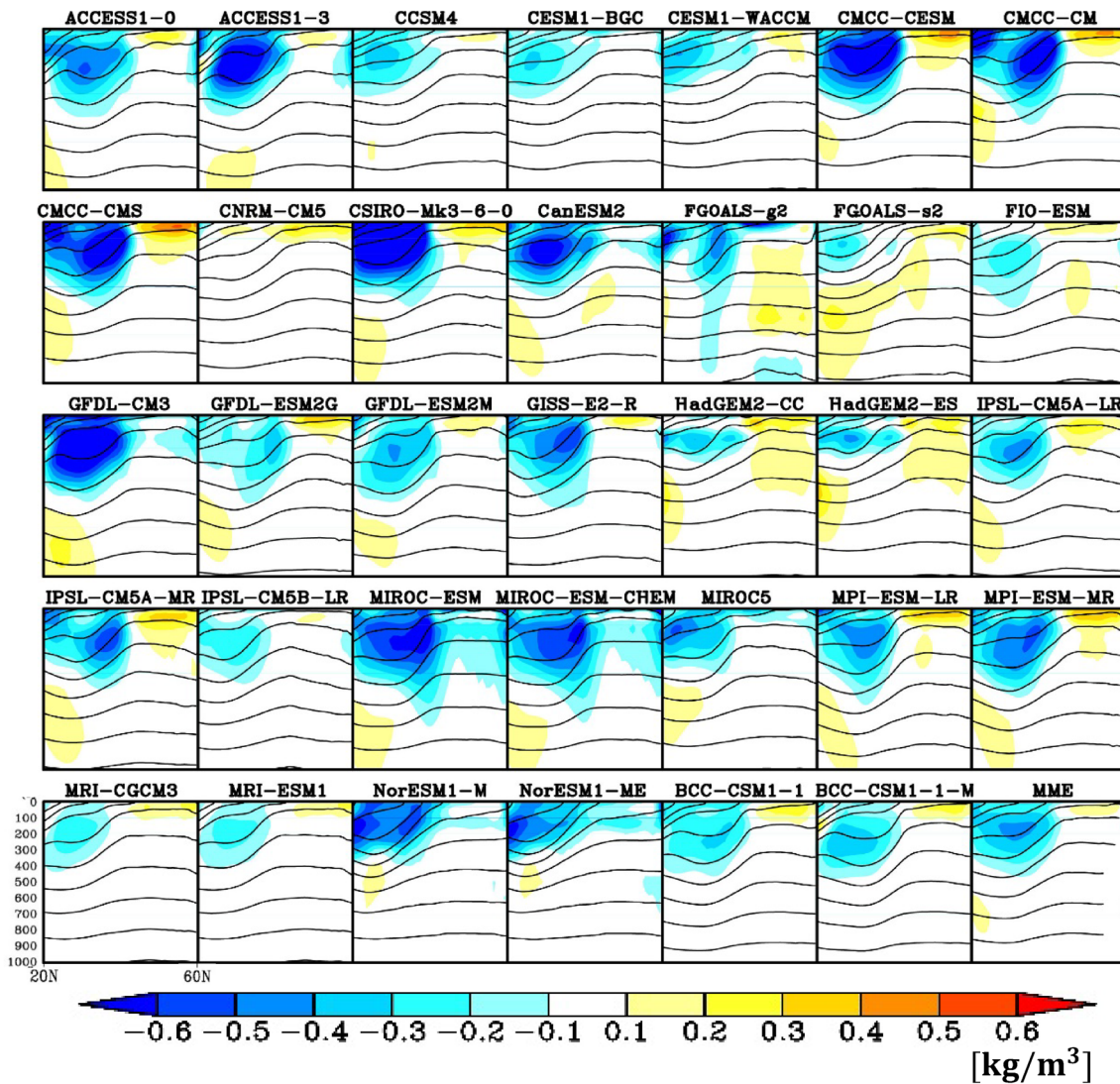


**Fig. 17** Zonally averaged ( $145^{\circ}$ – $170^{\circ}$ E) local density differences between 1971 and 2000 and 2071–2100 periods under RCP8.5 for each model (color). Contours indicate the mean  $\sigma$  for the period 1971–2000. MME indicates the MME mean

western North Pacific by 2100 and 2300. Specifically, the density decreases more strongly in the region of STMW than that around the KE axis until 2100 under both RCP4.5 and RCP8.5, whereas the density decreases more strongly around the KE axis than in the STMW region after 2100 under RCP8.5 (Fig. 4). The different patterns of density changes between the two periods result in the different spatial distributions of DSL changes by 2100 and 2300. The local density decrease in the STMW and the KE northward migration also explain different DSL changes among models (Figs. 6, 7). The KE migration is confirmed by subsurface geostrophic velocity analysis (Fig. 8). The KE exhibits not only a simple meridional migration but also a stronger concentration near the surface, probably due to enhanced stratification (Fig. 9).

The reduction in STMW density is likely to be caused at least in part by high heat uptake to the south and southeast of

Japan, where the Kuroshio and its extension flow (Figs. 10, 12). The excess heat flux in this region is very strongly related to the northward migration of the KE (Fig. 12). This northward KE shift is forced, at least in part, by changes in wind distribution, and the northward shift of the latitude of zero SSF results in northward shift of the KE (Figs. 13, 14). The poleward shift of the wind field is related to the poleward shift of the atmospheric circulation (Fig. 15), which is probably related to the poleward expansion of the Hadley circulation. The major features and mechanisms of DSL rise in the western North Pacific between 2000 and 2100 are summarized in Fig. 16.

As discussed in Sect. 1, previous studies suggest that the strong DSL rise in the western North Pacific around the KE is due to anomalous heat uptake, mainly due to STMW (Lowe and Gregory 2006; Suzuki and Ishii 2011b),

the northward migration of the KE (Sueyoshi and Yasuda 2012; Zhang et al. 2014) or KE intensification (Sueyoshi and Yasuda 2012). Among these three mechanisms, the first and last, anomalous heat uptake by the STMW and KE intensification may be closely associated. This is because the KE strength, defined by Sueyoshi and Yasuda (2012) as the meridional DSL difference between 34°N and 42°N for a 150°–165°E range, is the most likely to be dominated by a change in DSL at 34°N, which is within the meridional range of the STMW (Fig. 4). DSL change is much stronger at 34°N than at 42°N (Fig. 1), even using the composite difference for models that exhibit strong KE intensification (see Fig. 9 of Sueyoshi and Yasuda 2012). Consequently, we suggest that KE intensification may be better understood as an aspect of the heat uptake of STMW. This means that heat uptake by the STMW and meridional migration of the KE are the two essential mechanisms for DSL changes around the KE, though these two mechanisms are not totally independent, as shown by a significant correlation between the KE meridional migration and excess heat uptake to the south and southeast of Japan (Fig. 12).

The DSL changes attributable to these two mechanisms differ substantially among models. Figure 17 shows the local density difference for each model in the western North Pacific (145°–170°E) under RCP8.5. Most of the models exhibit local density differences for the STMW, but the magnitudes of the differences have wide variability, consistent with the situation in Fig. 5. Furthermore, many models (specifically, CMCC-CESM, CMC-CM, CMCC-CM5, FGOALS-g2, and IPSL-CM5A-MR) exhibit stronger changes associated with the KE, and some other models (CanESM2, hadGEM2-CC, HadGem2-ES, MIROC-ESM, MIROC-ESM-CHEM, MPI-ESM-MR) exhibit two maxima, corresponding to the STMW and the KE.

The inter-model differences of future response are bringing into question how these large inter-model differences are related to the mean state differences. To address this question, we apply the inter-model singular value decomposition (SVD) analysis that was used by Lyu et al. (2016) to examine the relationship between climatological mean state and interdecadal variability patterns among CMIP5 models. We first derive the departures of each model's DSL averaged for 1971–2000 period and the DSL difference between 1971 and 2000 and 2071–2100 periods from the MME mean patterns in the North Pacific (120°E–115°W, 20°N–60°N), and then apply the inter-model SVD analysis. The first mode explains only 12% of total variance, and there is no significant covariation in the western North Pacific where we focus on in this study. Therefore, the inter-model differences in the DSL rise around the KE is not well explained by the mean state difference. Future work is required for the better understanding of the reasons for model differences that would lead to better overall understanding and more certain projections.

**Acknowledgements** We thank Dr. Tatsuo Suzuki, Dr. Tamaki Yasuda, and Dr. Yoshi N. Sasaki for fruitful discussions. We also thank Dr. Tamaki Yasuda for providing some of the CMIP5 data used in this study. We acknowledge the climate modeling groups and the World Climate Research Programme's Working Group on Coupled Modelling for producing and making their model output available, and the US Department of Energy and other agencies contributing Earth System Grid Federation for their roles in collecting and archiving the model output. This work was supported by the Japan Society for the Promotion of Science (JSPS) KAKENHI Grant numbers 26287110, 26610146, and 15H01606.

## References

- Cheon WG, Park Y-G, Yeh S-W, Kim B-M (2012) Atmospheric impact on the northwestern Pacific under a global warming scenario. *Geophys Res Lett* 39:L16709. doi:10.1029/2012GL052364
- Church JA, Clark PU, Cazenave A, Gregory JM, Jevrejeva S, Levermann A, Merrifield MA, Milne GA, Nerem RS, Nunn PD, Payne AJ, Pfeffer WT, Stammer D, Unnikrishnan AS (2013) Sea level change. In: Stocker TF, Qin D, Plattner G-K, Tignor M, Allen SK, Boschung J, Nauels A, Xia Y, Bex V, Midgley PM (eds) *Climate change 2013: the physical science basis. Contribution of Working Group I to the Fifth Assessment Report of the Intergovernmental Panel on Climate Change*. Cambridge University Press, Cambridge
- Collins M, Knutti R, Arblaster J, Dufresne J-L, Fichetef T, Friedlingstein P, Gao X, Gutowski WJ, Johns T, Krinner G, Shongwe M, Tebaldi C, Weaver AJ, Wehner M (2013) Long-term climate change: projections, commitments and irreversibility. In: Stocker TF, Qin D, Plattner G-K, Tignor M, Allen SK, Boschung J, Nauels A, Xia Y, Bex V, Midgley PM (eds) *Climate change 2013: the physical science basis. Contribution of Working Group I to the Fifth Assessment Report of the Intergovernmental Panel on Climate Change*. Cambridge University Press, Cambridge
- Frierson DMW, Lu J, Chen G (2007) Width of the Hadley cell in simple and comprehensive general circulation models. *Geophys Res Lett* 34:L18804. doi:10.1029/2007GL031115
- Gan B, Wu L, Jia F, Li S, Cai W, Nakamura H, Alexander MA, Miller AJ (2017) On the response of the Aleutian low to greenhouse warming. *J Clim* 30:3907–3925. doi:10.1175/JCLI-D-15-0789.1
- Gregory JM et al (2001) Comparison of results from several AOGCMs for global and regional sea-level change 1900–2100. *Clim Dyn* 18:225–240
- Hu Y, Tao L, Liu J (2013) Poleward expansion of the hadley circulation in CMIP5 simulations. *Adv Atmos Sci* 30:790–795
- Ishii M, Kimoto M (2009) Reevaluation of historical ocean heat content variations with time-varying XBT and MBT depth bias corrections. *J Oceanogr* 65:287–299
- Johanson CM, Fu Q (2009) Hadley cell widening: model simulations versus observations. *J Clim* 22:2713–2725
- Liddicoat S, Jones C, Robertson E (2013) CO<sub>2</sub> emissions determined by HadGEM2-ES to be compatible with the representative concentration pathway scenarios and their extensions. *J Clim* 26:4381–4397
- Liu Z-J, Minobe S, Sasaki YN, Terada M (2016) Dynamical downscaling of future sea-level change in the western North Pacific using ROMS. *J Oceanogr* 72:905–922. doi:10.1007/s10872-016-0390-0
- Lowe JA, Gregory JM (2006) Understanding projections of sea level rise in a Hadley Centre coupled climate model. *J Geophys Res* 111:C111014. doi:10.1029/2005JC003421
- Lu J, Vecchi GA, Reichler T (2007) Expansion of the Hadley cell under global warming. *Geophys Res Lett* 34:L06805. doi:10.1029/2006GL028443



- Luo YY, Liu QY, Rothstein LM (2009) Simulated response of North Pacific Mode Waters to global warming. *Geophys Res Lett* 36:L23609. doi:[10.1029/2009GL040906](https://doi.org/10.1029/2009GL040906)
- Lyu K, Zhang X, Church JA, Hu J (2016) Evaluation of the interdecadal variability of sea surface temperature and sea level in the Pacific in CMIP3 and CMIP5 models. *Int J Climatol* 36:3723–3740. doi:[10.1002/joc.4587](https://doi.org/10.1002/joc.4587)
- Miller RL, Schmidt GA, Shindell DT (2006) Forced annular variations in the 20th century Intergovernmental Panel on Climate Change Fourth Assessment Report models. *J Geophys Res* 111:D18101
- Mitrovica JX, Gomez N, Morrow E, Hay C, Latychev K, Tamisiea ME (2011) On the robustness of predictions of sea level fingerprints. *Geophys J Int* 187:729–742
- Nicholls RJ, Hanson SE, Lowe JA, Warrick RA, Lu X, Long AJ (2014) Sea-level scenarios for evaluating coastal impacts. *WIREs Clim Change* 2014 5:129–150. doi:[10.1002/wcc.253](https://doi.org/10.1002/wcc.253)
- Oshima K, Tanimoto Y, Xie S-P (2012) Regional patterns of winter-time SLP change over the North Pacific and their uncertainty in CMIP3 multi-model projections. *J Meteorol Soc Jpn* 90A(0):385–396. doi:[10.2151/jmsj.2012-A23](https://doi.org/10.2151/jmsj.2012-A23)
- Pardaens AK, Gregory JM, Lowe JA (2010) A model study of factors influencing projected changes in regional sea level over the twenty-first century. *Clim Dyn* 36:2015–2033
- Peltier WR (2004) Global glacial isostasy and the surface of the ice-age earth: the ICE-5G (VM2) model and GRACE. *Annu Rev Earth Planet Sci* 32:111–149
- Previdi M, Liepert BG (2007) Annular modes and Hadley cell expansion under global warming. *Geophys Res Lett* 34:L22701. doi:[10.1029/2007GL031243](https://doi.org/10.1029/2007GL031243)
- Rauthe M, Hense A, Paeth H (2004) A model intercomparison study of climate change-signals in extratropical circulation. *Int J Clim* 24:643–662
- Slangen ABA, Carson M, Katsman CA, van de Wal RSW, Köhl A, Vermeersen LLA, Stammer D (2014) Projecting twenty-first century regional sea-level changes. *Clim Change* 124:317–332. doi:[10.1007/s10584-014-1080-9](https://doi.org/10.1007/s10584-014-1080-9)
- Sueyoshi M, Yasuda T (2012) Inter-model variability of projected sea level changes in the western North Pacific in CMIP3 coupled climate models. *J Oceanogr* 68:533–543
- Sugimoto S, Hanawa K, Watanabe T, Suga T, Xie S-P (2017) Enhanced warming of the subtropical mode water in the North Pacific and North Atlantic. *Nat Clim Change* 7:656–658. doi:[10.1038/nclimate3371](https://doi.org/10.1038/nclimate3371)
- Suzuki T, Ishii M (2011a) Long-term regional sea level changes due to variations in water mass density during the period 1981–2007. *Geophys Res Lett* 38:L21604. doi:[10.1029/2011GL049326](https://doi.org/10.1029/2011GL049326)
- Suzuki T, Ishii M (2011b) Regional distribution of sea level changes resulting from enhanced greenhouse warming in the Model for Interdisciplinary Research on Climate version 3.2. *Geophys Res Lett* 38:L02601. doi:[10.1029/2010GL045693](https://doi.org/10.1029/2010GL045693)
- Taylor KE, Stouffer RJ, Meehl GA (2012) An overview of CMIP5 and the experiment design. *Bull Amer Meteorol Soc* 93:485–498. doi:[10.1175/BAMS-D-11-00094.1](https://doi.org/10.1175/BAMS-D-11-00094.1)
- Thomson AM, Calvin KV, Smith SJ et al (2011) RCP4.5: a pathway for stabilization of radiative forcing by 2100. *Clim Change* 109:77. doi:[10.1007/s10584-011-0151-4](https://doi.org/10.1007/s10584-011-0151-4)
- Timmermann A, McGregor S, Jin F-F (2010) Wind effects on past and future regional sea level trends in the Southern Indo-Pacific. *J Clim* 23:4429–4437
- Wada Y, van Beek LPH, Sperna Weiland FC, Chao BF, Wu Y-H, Bierkens MFP (2012) Past and future contribution of global groundwater depletion to sea-level rise. *Geophys Res Lett* 39:L09402. doi:[10.1029/2012GL051230](https://doi.org/10.1029/2012GL051230)
- Willis JK, Church JA (2012) Climate change. Regional sea-level projection. *Science* 336:550–551
- Yin J (2012) Century to multi-century sea level rise projections from CMIP5 models. *Geophys Res Lett* 39:L17709. doi:[10.1029/2012GL052947](https://doi.org/10.1029/2012GL052947)
- Yin J, Griffies SM, Stouffer RJ (2010) Spatial variability of sea level rise in twenty-first century. *Project J Clim* 23:4585–4607
- Zhang X, Church JA, Platten SM, Monselesan D (2014) Projection of subtropical gyre circulation and associated sea level changes in the Pacific based on CMIP3 climate models. *Clim Dyn* 43:131–144